Parallel Simulation of Cellular Flow in Microvessels Using a Particle Method*

Davod ALIZADEHRAD**, Yohsuke IMAI***, Keita NAKAAKI***,
Takuji ISHIKAWA*** and Takami YAMAGUCHI**

**Department of Biomedical Engineering, Tohoku University,
6-6-01 Aramaki Aza Aoba, Sendai 980-8579, Japan
E-mail: yimai@pfsl.mech.tohoku.ac.jp
*** Department of Bioengineering and Robotics, Tohoku University

Abstract

We developed a numerical method for large-scale simulations of cellular flow in microvessels. We employed a particle method, where all blood components were modeled using a finite number of particles. Red blood cell deformation was modeled by a spring network of membrane particles. A domain decomposition method was used for parallel implementation on distributed memory systems. In a strong scaling test up to 64 CPU cores, we obtained a linear speedup with the number of CPU cores, and demonstrated that our model can simulate $O(10^3)$ red blood cells in vessels a few tens of micrometers in diameter. For quantitative validation, we analyzed the Fåhræus effect and the formation of a cell-depleted peripheral layer. Simulations were performed for tube hematocrit ranging from 20 to 45%, and microvessel diameters from 9 to 50 μm. Our numerical results were in good agreement with previous experimental results both for the discharge hematocrit and cell-depleted peripheral layer thickness.

Key words: Large-Scale Simulation, Red Blood Cell, Microcirculation, Cell-Depleted Peripheral Layer, Fåhræus Effect

1. Introduction

In blood vessels with diameters larger than 300 μm, blood may be modeled as a homogeneous fluid; however, in small vessels, *i.e.* capillaries, arterioles, and venules, the particulate nature of blood becomes more apparent, and individual cell motion affects blood flow. Red blood cells (RBCs) are the most important constituent of blood in terms of rheology, and comprises a 20 to 45% volume fraction of blood. Recent confocal microscopy with microfluidics has improved experimental measurements of RBC behavior in microvessels. However, owing to light scattering by RBCs and light absorption by hemoglobin, RBCs can be observed only under low hematocrit condition ($Hct < 20\%$)[1,2].

Numerical modeling, however, can further our understanding of the many physiological and pathological processes in microcirculation. It is important to simulate blood flow based on cellular scale modeling; hence, we must model RBCs explicitly. An RBC is a highly deformable, biconcave-shaped cell with a high surface to volume ratio. It contains the Newtonian solution hemoglobin, whose viscosity is several times that of blood plasma[3]. The membrane of an RBC consists of a lipid bilayer underlined by a spectrin network[4,5], which exhibits resistance to shear and bending[6]. This is a fluid-structure interaction problem, where the solid mechanics of the membrane must be coupled with the fluid mechanics of the cytoplasm (interior liquid) and plasma (exterior liquid). It requires

fine computational meshes smaller than the cell size. Consequently, the computational power required to simulate blood flow increases with vessel diameter.

Recently, some research groups have developed numerical methods for simulating the three-dimensional flow of multiple RBCs through microvessels. Doddi and Bagchi[7] employed a front tracking method to simulate the flow of biconcave capsules in channels with a hematocrit up to 27%. Dupin et al.[8] employed a lattice Boltzmann method (LBM) to simulate 200 RBCs in a rectangular channel. Zhao and coworkers analyzed a few tens of RBCs flowing in microvessels up to 17 μm in diameter by utilizing a boundary integral method (BIM)[9]. Fedosov et al.[10] investigated the formation of a cell-depleted peripheral layer (CDPL) in microvessels up to 40 μm using a dissipative particle dynamics (DPD)[11] method with a coarse-grained model of RBCs [12,13]. McWhirter et al.[14] modeled vesicles within a multiparticle collision dynamics framework[15]. Despite the progress in blood flow modeling and promising results, high computational expense remains a major problem, particularly when blood flow in vessels with diameters of tens or hundreds of micrometers is simulated, involving hundreds or thousands of RBCs. Alternatively, two-dimensional simulations have been used for vessels that are hundreds of micrometers in diameter [16].

A number of models of blood flow based on particle methods have been proposed[17,18]. We also developed a numerical model based on the particle method, and successfully applied it to studies of malaria infection[19,20] and primary thrombogenesis[21]. While this method has the potential to simulate complex blood flow induced by multiple RBCs, coupled with intercellular biochemical interactions, the large computational load has limited us to simulating blood flow only in small vessels ($D \sim 12$ μm). To progress further, development of a computational procedure to overcome this problem is necessary.

The first objective of this study was to develop a highly scalable parallel implementation of our method on distributed memory systems, towards large-scale simulations including $O(10^3)$ RBCs. While this model was validated at the cellular scale, it is still unclear whether it can simulate blood flow in vessels that are tens of micrometers in diameter. Hence, the second objective was to validate the accuracy for microvascular flow, through analysis of the Fåhræus effect[22] and the cell-depleted peripheral layer.

2. Methods

2.1. Numerical model

Detailed information on the model can be found in our previous paper[19]. Herein, we provide a brief review. All blood components, including plasma, cytoplasm and membranes are modeled using a finite number of particles. Each particle has physical quantities such as position, velocity, and viscosity. An RBC is modeled as an initially biconcave cell[23], consisting of membrane particles and cytoplasm particles. A triangular network of membrane particles are constructed, where neighboring particles are connected by a linear spring to represent the elastic property of RBCs. Bending resistance between neighboring elements is also considered. Assuming that the plasma and cytoplasm are incompressible and viscous fluids, particle motion is governed by the conservation laws of mass and momentum as:

$$\frac{D\rho}{Dt} = 0 , \tag{1}$$

$$\rho \frac{D\mathbf{u}}{Dt} = -\nabla p + \mu \nabla^2 \mathbf{u} + \mathbf{f} , \tag{2}$$

where t refers to the time, ρ the density, $\mathbf{u}$ the velocity, p the pressure, μ the dynamic

viscosity, *D/Dt* the Lagrangian derivative, and **f** the external force. We used a moving particle semi-implicit (MPS) method[24] to discretize the governing equations. In the MPS method, the momentum equation is split into an advection-diffusion equation and a Poisson equation for pressure. The incompressibility is expressed by the particle number density, implicitly combined with the Poisson equation. Forces generated by the stretching/compression and bending of the membrane are substituted into the external force term **f** for membrane particles only. Since the motion of membrane particles are directly solved by Eqs. (1) and (2), the hydrodynamic interaction between RBCs as well as that between an RBC and the wall is automatically computed, and the no-slip condition at the membrane is satisfied in this procedure. In our previous paper[19], this model was confirmed to simulate the deformation of RBCs by optical tweezers stretching[25] and deformation in shear flow[26], including in *Plasmodium falciparum* malaria infection.

2.2. Parallel algorithm

Distributed memory systems are configured so that some memory is local to each processor, which is not globally accessible. The only way to share data among processors is to send data explicitly from one processor to another. This is called the message-passing model[27]. Therefore, in contrast to shared memory systems, performance depends on how well the algorithm is designed. One of the most important points in parallel computing is to balance computational load and minimize communication among processors[28]. We used a domain decomposition method to distribute global computational load to local processors (CPU cores). Computational domain is geometrically divided into several sub-domains with approximately equal computational expenses; these sub-domains are distributed among parallel processors. In particle methods, the position of a particle changes considerably over time, and subsequently, it can move from one processor to another. Hence, in general, domain partitioning does not guarantee load balancing for parallel computation of particle methods. However, in the case of flow in vessels, the MPS method guarantees that the number of particles in a sub-domain does not significantly change over time, because the mass conservation is expressed by the constant number density of particles.

In this paper, we used one-dimensional (1D) partitioning; however, extension to two-dimensional (2D) and three-dimensional (3D) partitioning is straightforward. Figure 1 shows communication between two neighboring processors. In the MPS method, the gradient and Laplacian operators are discretized by interaction models between particles[24], and the radius of the interaction is bounded by the kernel size (r_e). Thus, the particles located on or near the inter-processor-boundary (IPB) need information on ghost zone particles. These ghost zone particles are equivalent to particles near the ghost zone in the neighboring processor (rank), hence a list of particles near the ghost zone is created in all processors. The information of these particles is then shared among the neighboring ranks through a single-packed message and MPI_SENDRECV operation[27]. Since processes need to communicate mainly with their nearest neighbors, we created a virtual Cartesian communicator between processors using MPI_CART_CREATE and MPI_CART_SHIFT functions[27,28] to optimize communication. This communicator also enables us to easily implement a periodic boundary condition between the inlet and outlet of the vessel. Dynamic load balancing can be performed by small displacement of IPB to control the number of particles in each processor sub-domain. Processors periodically exchange information on ghost regions as the computation advances.
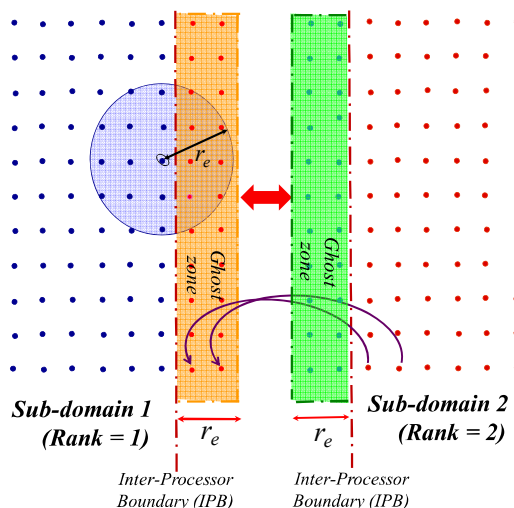
Fig. 1 A schematic of communication between two processors

Another problem in parallel implementation arises from RBCs. Figure 2 shows an example of 1D partitioning to 40 sub-domains. Since an RBC usually locates at several processors, recognition of each sub-part and communication for the computation of membrane forces are needed. In our model, the network of membrane particles is identical for all RBCs to avoid sending connectivity information. We set the index of membrane particles in a fixed order, which enables automatic recognition of connectivity by each processor. When an RBC crosses an IPB for the first time and enters a new processor domain, we allocate memory for all membrane particles of that RBC. Additionally, in the new sub-domain, a local index (name) is assigned to this RBC, which is shared among those neighboring processors that contain a part of this RBC. This local index is used to recognize RBC parts in several processor sub-domains. The information on RBC particles in the IPB is sent in the same manner as fluid particles and stored with the assigned order of the index. Memory allocated to the RBC that exited for the next processor is then used for newly entering RBC.
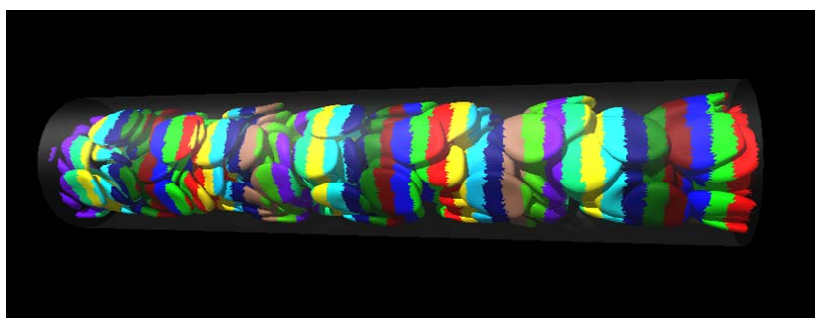

Fig. 2 Domain decomposition for parallel computing. When two membrane particles of a triangle are located in a sub-domain, the triangle is colored for this sub-domain.

To avoid large memory allocation in processors, the computational domain is partitioned using a serial pre-processing program, and the information of that sub-domain is input into processors. Briefly, the simulation procedure is as follows: first, the viscous and elastic force terms are calculated, where the viscous term is solved implicitly by using a

parallel incomplete Cholesky conjugate gradient (ICCG) algorithm with collective and non-blocking communications.   Then, the intermediate velocity and position are updated in each processor sub-domain, and the new information on ghost region particles is communicated.   To solve the linear system with a sparse matrix, which arises from the pressure Poisson equation, we developed a parallel bi-conjugate gradient stabilized (BiCGstab) iterative solver.   Velocity and position of the particles are corrected using the pressure gradient term.   Finally, information on particles that crossed IPB is communicated again.

3. Results and Discussion

We simulated blood flow in a circular channel with a diameter D and a length L. Boundary conditions were no-slip at the wall and a periodic boundary condition at the inlet and outlet.   To drive flow in the vessel, a pressure difference Δp was given between the inlet and outlet.   Initially, RBCs were distributed randomly throughout the channel.   In this paper, the density of all particles was $\rho = 1.0 \times 10^3$ kg/m^3, the viscosity of plasma was $\mu_p = 1.3 \times 10^{-3}$ Pas, and that of cytoplasm was $\mu_c = 8.0 \times 10^{-3}$ Pas.   For the viscosity of the membrane, we used the averaged value, $\mu_m = (\mu_p + \mu_c)/2$.   The healthy RBC model proposed in Imai et al.[19] was employed in this study (see Imai et al.[19] in detail).   Each simulation was run for a sufficient enough time to remove the effects of the initial transition and to analyze the data over time at an almost quasi-steady state.   Even at the quasi-steady state, small fluctuation inherently occurs in time due to the motion of RBCs.   Figure 3 shows an example of the fluctuation of cell-depleted peripheral layer thickness.   The tendency in the time histories were almost the same for all the cases in this study, we hence averaged values after 0.3 s for a quasi-steady state.

We examined cases of the diameters ranging from 9 to 50 μm and hematocrits, $Hct = 20, 30$ and 45%.   For each diameter, a fixed pressure difference was given between the inlet and outlet, and then pseudo shear rate, $\gamma = U/D$, was in the range of 60 s^{-1} to 120 s^{-1}, where U is the average velocity.
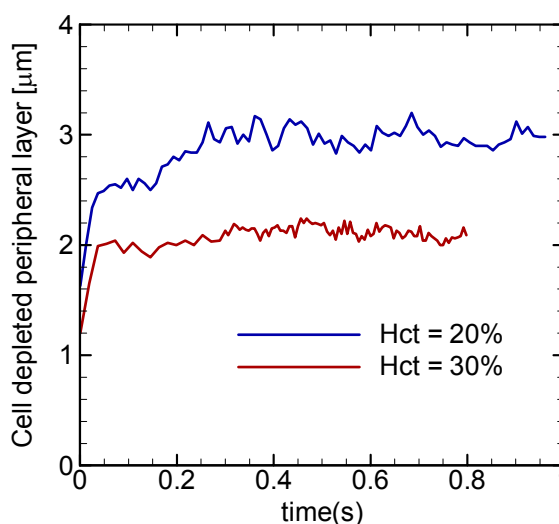

Fig. 3 Time histories of cell-depleted peripheral layer thickness for $D = 19$ μm.

3.1. Performance of parallel computations

We evaluated the strong scaling of our parallel computations, in which a fixed number of total particles was solved, while the number of CPU cores increased. We simulated conditions of $D = 25$ μm, $L = 120$ μm, and $Hct = 30\%$, where 160 RBCs were included and the total number of particles was approximately 1,200,000. Speedup is defined as the ratio of the computational time with a reference number of CPU cores to that with a given number of CPU cores. We used a CPU cluster connected with a Gigabit Ethernet, in which each node had two CPUs, Quad-core Intel Xeon X5570. Since a computation with less than 8 CPU cores does not require communication through the Ethernet connection, we set the reference number at 8 CPU cores. The speedup is presented in Fig. 4, where the ideal linear speedup and the speedup for plasma flow (without RBCs) are also shown. The speedup for blood flow shows an almost linear relationship with the given number of CPU cores up to at least 64 cores, specifically, compared with 8 cores, a 7-fold speedup was achieved with 64 cores, which was almost the same as that for the plasma flow. This result indicates the high efficiency of the developed parallel algorithm for particle-based modeling of blood flow. This enables us to simulate blood flow at a higher hematocrit in larger microvessels. For example, Fig. 5 shows a snapshots of a blood flow simulation for $Hct = 45\%$ and $D = 50$ μm, wherein approximately 1000 RBCs and a total number of 6,000,000 particles were solved. As shown in Fig. 5b, we could visualize the shapes of RBCs in the center of the vessel, when the domain was cut in the central plane. Such an image is difficult to obtain experimentally due to light absorption by hemoglobin and light scattering by RBCs.
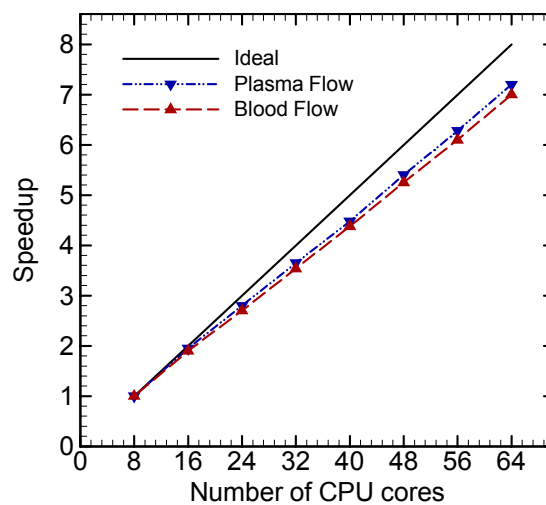

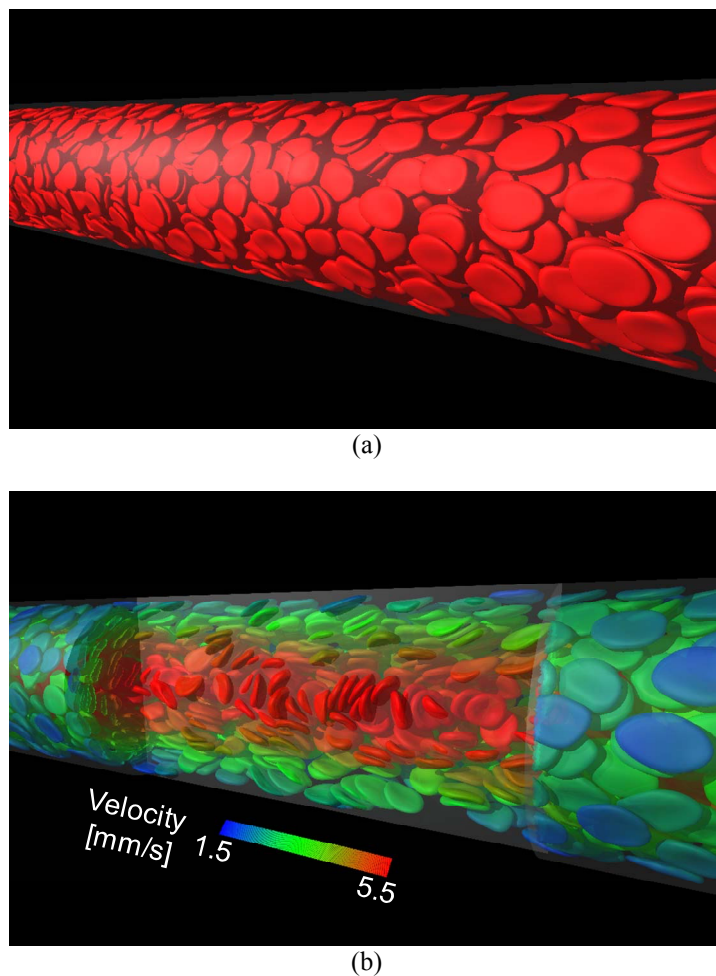Fig. 4 Speedup with the number of CPU cores

(a)

Velocity [mm/s] 1.5 5.5

(b)

Fig. 5 An example of a large-scale simulation for D = 50 μm and Hct = 45%: (a) A snapshot of typical RBCs. (b) The domain is cut in the central plane of the vessel, and colors represent the local velocity.

3.2. Fåhræus effect

To quantitatively validate the numerical model, we analyzed the Fåhræus effect. The Fåhræus effect here refers to discharge hematocrit (Hct_D) at the outlet of a microvessel being higher than the hematocrit in the microvessel (tube hematocrit, Hct)[22]. This phenomenon ($Hct < Hct_D$) results from the coupling effect of axial migration of RBCs and velocity profile in the vessel. The axial migration of RBCs leads to hematocrit variation in the radial position (local hematocrit, Hct_L) and the formation of a cell-depleted peripheral layer (CDPL) near the wall. Because of the slow velocity near the wall, the average velocity of RBCs becomes faster than the suspension velocity[29].

In a given time interval, particles, *i.e.* plasma, membrane, and cytoplasm particles exit from the vessel. When the number of these particles is defined as N_p (plasma), N_m (membrane), and N_c (cytoplasm), the value of Hct_D is calculated by:

$$Hct_D = \frac{N_m + N_c}{N_p + N_m + N_c} .$$
(3)

Pries et al.[30] proposed an empirical expression of Hct_D as a function of D and Hct:

$$\frac{Hct}{Hct_D} = Hct_D + \left(1 - Hct_D\right)\left(1 + 1.7e^{-0.35D} - 0.6e^{-0.01D}\right).$$ (4)

A comparison of numerical results and empirical expression is presented in Fig. 6. Numerical results are in good agreement with the empirical expression for a wide range of vessel diameters and Hct values. As shown in the figure, Hct_D decreases when the microvessel diameter increases from 9 to 50 μm. A general tendency of the discharge hematocrit is $Hct_D > Hct$, where Hct_D reaches ~55% for $Hct = 45$%. However, when we consider a ratio of the discharge hematocrit to the tube hematocrit, Hct_D/Hct, a lower tube hematocrit results in a higher ratio. For example, in the case of $D = 37$ μm, $Hct_D/Hct = 1.23$ for $Hct = 45$%, but $Hct_D/Hct = 1.42$ for $Hct = 20$%.
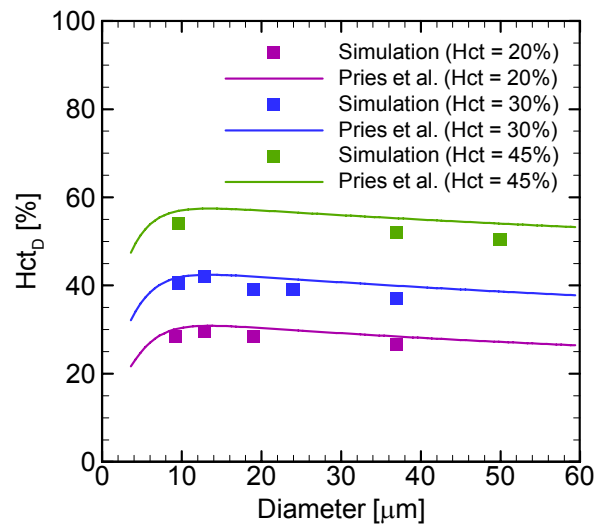

Fig. 6 Comparison of discharge hematocrit between numerical and experimental[30] results

To further study the Fåhræus effect, the local hematocrit and velocity profiles were analyzed. Instantaneous distributions of RBCs are shown in Fig. 7 and Fig. 8 for $D = 19$ μm and 37 μm, respectively. A thinner CDPL resulted from a higher tube hematocrit condition. We calculated the radial variation of the local hematocrit (Hct_L) as

$$Hct_L(r) = \frac{N_m(r) + N_c(r)}{N_p(r) + N_m(r) + N_c(r)},$$ (5)

where r is the radial position, and $N(r)$ is the number of particles located at a radial position within $r \pm 0.5$ μm. We first calculated an instantaneous value of the local hematocrit at each time t, and then we averaged the values over the time. Figure 9 shows the radial variation in Hct_L/Hct. When $D = 19$μm and $Hct = 20$%, the local hematocrit is 2.5 times larger than the tube hematocrit ($Hct_L/Hct > 2.5$) at the center of the vessel. The local hematocrit decreases toward the CDPL with a sharp drop near the CDPL. A similar tendency was observed in a numerical study by Freund et al.[31], in which blood flow for

D = 11.3 μm and Hct = 30% was simulated by BIM.   For D = 37 μm and Hct = 20%, the tendency was identical, and $Hct_L/Hct > 2.0$ at the center of the vessel.   When the tube hematocrit increases, the local hematocrit distribution becomes flatter with a decrease in the CDPL, resulting in a smaller Hct_L/Hct value in the center of the vessel.   In the case of D = 37μm and Hct = 45%, $Hct_L > 63\%$ in the center of the vessel, while Hct_L remained 42% for Hct = 20%.   This suggests that RBCs were pushed together away from the center in the high hematocrit condition.
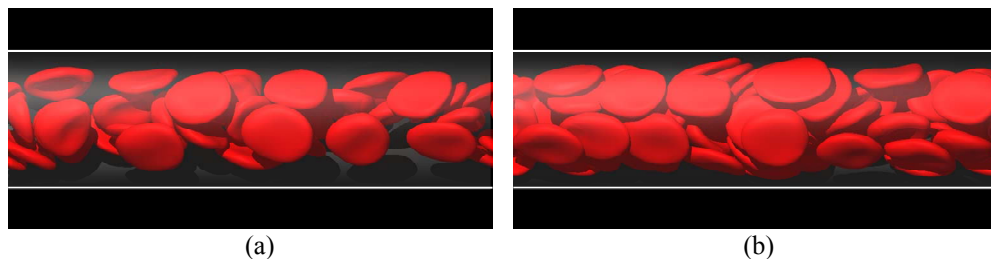

(a)   (b)

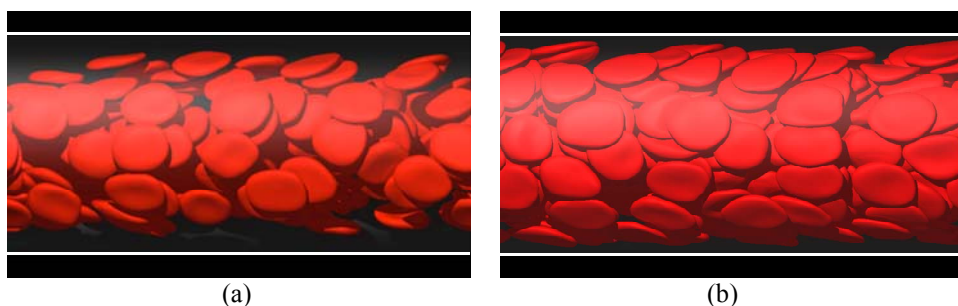Fig. 7 Snapshots of blood flow for D = 19 μm: (a) Hct = 20%; (b) Hct = 30%.

(a)   (b)

Fig. 8 Snapshots of blood flow for D = 37 μm: (a) Hct = 20%; (b) Hct = 45%.
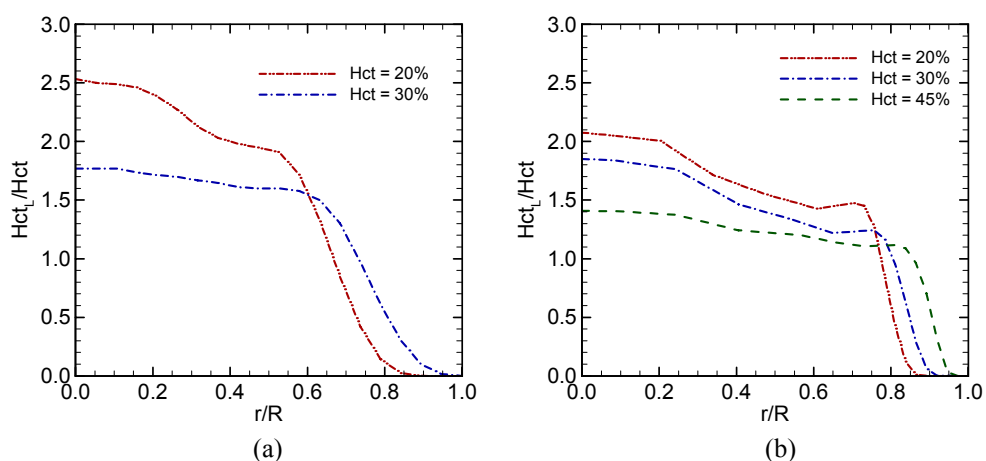

(a)   (b)

Fig. 9 Radial distribution of Hct_L/Hct: (a) D = 19μm; (b) D = 37 μm.

While the local hematocrit profile depends strongly on the tube hematocrit, the velocity profile is relatively unaffected.   Radial variation in velocity is presented in Fig. 10, where the velocity is normalized to the maximum velocity in each case.   The velocity near the

center of the vessel exhibited a flat (plug flow) profile; however the velocity near the wall had a steep gradient, which matched the velocity gradient of Poiseuille flow if we did not normalize. The overall velocity profile differed significantly from the Poiseuille flow profile of plasma flow. With increasing *Hct*, the velocity profile became a more blunt profile in the RBC region, but the difference was not so large for 20% ≤ *Hct* ≤ 45%. In particular, the velocity profiles were almost identical between *Hct* = 30% and *Hct* = 45% for *D* = 37μm. These results indicate that lower tube hematocrit conditions cause a thicker CDPL and a higher ratio of local hematocrit to tube hematocrit (Hct_L/*Hct*) in the RBC region, maintaining the velocity profile. This phenomenon results in the higher ratio of discharge hematocrit to tube hematocrit (Hct_D/*Hct*) at lower tube hematocrit conditions.
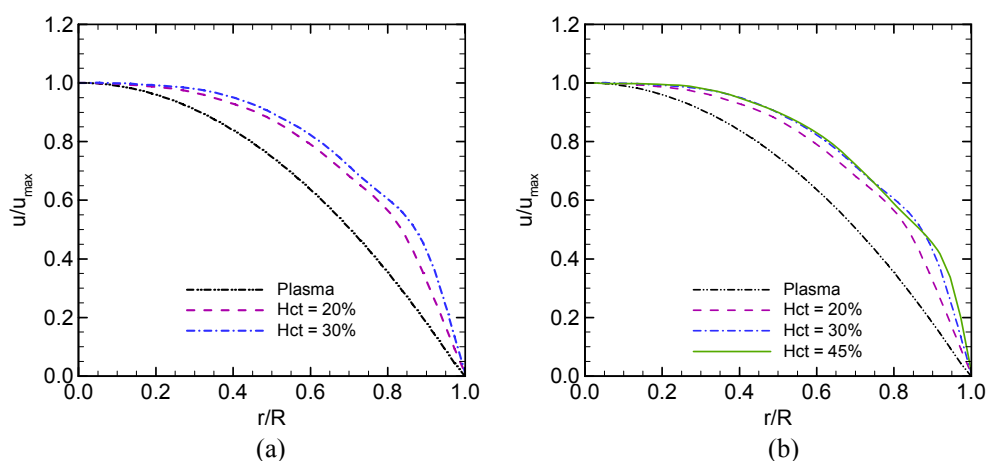

Fig. 10 Velocity profile normalized by the maximum velocity: (a) *D* = 19μm; (b) *D* = 37 μm.

3.3. Cell-depleted peripheral layer

As shown in the previous section, the thickness of the CDPL was linked directly to the Fåhræus effect. We therefore checked the accuracy of the predicted CDPL thickness by comparing with experimental results. To calculate the CDPL thickness from the simulation, we measured the distance between the outermost edge of RBCs and the wall, which was similar to previous experimental procedures[32-34]. The outermost edge was actually indistinct and irregular in experiments[35,36]. It also exhibited spatial and temporal fluctuations in numerical simulations because of the dispersive effect of interactions between deformable cells. Therefore, the vessel was divided into small segments in both the flow and angular directions, and the CDPL thickness over all segments and time was averaged.

We compared the numerical results with the experimental results *in vivo* [32,36] and *in vitro*[37,38] (Fig. 11). First, the results of our simulations were in almost perfect agreement with the *in vivo* work of Tateishi *et al.*[32], in which a perfused isolated rabbit mesentery was used. However in our simulation, the microvessel wall was assumed to be rigid, while the *in vivo* experiment had an elastic wall. Maeda *et al.*[33] reported that the CDPL of an elastic vessel was 0.4 μm thinner than that of the hardened vessel at high hematocrits (30% ≤ *Hct* ≤ 45%), but thicker than the hardened vessel at low hematocrits (*Hct* = 8%). The perfectly matched results may indicate that our model includes a slight difference from the expected values, for example, a 0.4 μm larger value might be expected for *Hct* = 30 and 45% under the current rigid wall conditions. Although the 0.4 μm-difference demonstrates

the accuracy of our model, the CDPL measured *in vivo* may include the glycocalyx layer, which is of 0.4-0.5 μm thickness. When the glycocalyx layer is considered in the *in vivo* experiment, the results of Tateishi *et al*. may be increased by 0.4-0.5 μm. The expected values would then be similar to our predicted values.

Next, we compared the results with *in vitro* experiments. Although we defined *Hct* by the tube hematocrit, the results *in vitro* presented by Bugliarello and Sevilla[37] and Reinke *et al*.[38] were based on the discharge hematocrit (Hct_D). When we apply Eq. (4) by Pries *et al*.[39] to these Hct_D values, the corresponding tube hematocrits are Hct = 30% for Bugliarello and Sevilla (D = 40 μm) and Hct = 34% for Reinke *et al* (D = 30.8 μm). On the other hand, in our model at Hct = 30%, Hct_D = 39% was predicted for D = 24 μm, and Hct_D = 37% for D = 37 μm (Fig. 6). Therefore, when the differences between the tube and discharge hematocrits are taken into account, our results show good agreement with these *in vitro* experiments.

While our model shows good agreement with the above-mentioned *in vivo* and *in vitro* experiments, a significant difference from *in vivo* work of Kim *et al*.[36] was detected. Their results also differ from that of others, likely due to the use of systemic hematocrit (Hct_S). They measured the CDPL thickness for Hct_S = 42% in rat cremaster muscle. However, concentration of RBCs is known to decrease with decreasing vessel diameter, which is also referred to the Fåhræus effect[40,41]; therefore, it is difficult to directly convert Hct_S into Hct or Hct_D. Kim *et al*. compared their obtained CDPL thickness with the *in vitro* result of Hct_D = 45% by Reinke *et al*.[38] for D = 31 μm, 58 μm. They found 0.3μm increases in thickness *in vivo*, and concluded that this was due to the absence of the glycocalyx *in vitro*. Note that our predicted values for Hct = 30% were in-between those of Reinke *et al*.[38] and Kim *et al*.[36]

We also compared these results with previous numerical results. While the DPD method of Fedosov *et al*.[10] predicted a slightly thicker CDPL than ours in all cases, the BIM used by Freund *et al*.[31] generated results that matched our own.

Note that aggregation of RBCs was not modeled in the simulations. Reinke *et al*.[38] compared the CDPL between plasma, dextran, and saline solutions. They demonstrated no significant effect of the aggregation on the CDPL thickness for high shear rates, which were estimated at $γ$ > 50 s⁻¹. The above-mentioned experimental studies also used shear rates similar to ours, although Kim *et al*.[36] used a slightly higher value for small diameter vessels (D < 30 μm) to prevent aggregation. Hence, the effect of aggregation can be ignored in the current analysis.

It is also noted that in non-aggregating conditions, when we increased the shear rate from 30 to 90 s⁻¹ for D = 37 μm, the CDPL thickness increased only by 0.3 μm on average as shown in Fig. 11, where the blue open symbols represent the results for $γ$ = 30 s⁻¹. The CDPL thickness became approximately constant around $γ$ = 90 s⁻¹. Although the numerical model of Fedosov *et al*.[10] predicted a decrease in the CDPL with increasing shear rate, other studies demonstrated the same tendency as ours, including a numerical simulation[31] and experiments *in vitro*[38] for the shear rate investigated. Therefore, small variations in the shear rate would not affect the result.
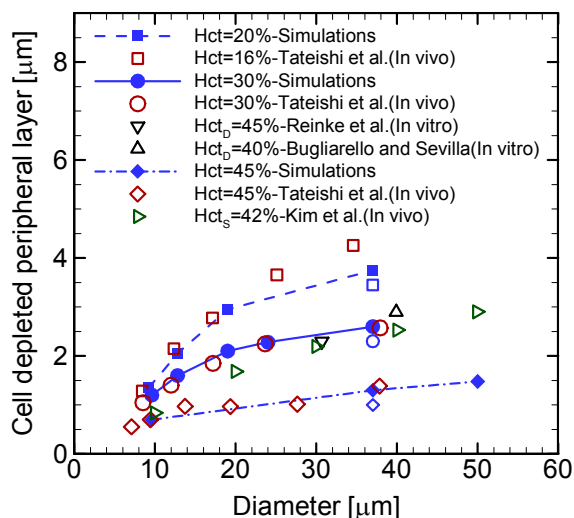
Fig. 11 Cell-depleted peripheral layer thickness as a function of microvessel diameter. Blue open symbols at $D = 37$ μm represent the results for $\gamma = 30$ s^{-1}.

4. Conclusions

We have presented here a computational method for large-scale simulation of blood flow in microcirculation. In our method, all blood components were represented by a finite number of particles. A two-dimensional spring network of membrane particles was constructed to model the deformation of RBCs. We developed a parallel implementation of this method on distributed memory systems using a domain decomposition technique. In a strong scaling test up to 64 CPU cores, we obtained a linear speedup with the number of CPU cores, and demonstrated that our model can simulate $O(10^3)$ RBCs in vessels a few tens of micrometers in diameter. For quantitative validation, we analyzed the Fåhræus effect and CDPL formation. Simulations were performed for tube hematocrits ranging from 20 to 45%, and microvessel diameters from 9 to 50 μm. Our numerical results were in good agreement with previous experimental results for both the discharge hematocrit and the CDPL thickness. Experiments have failed to observe RBC behavior in the center of microvessels in a dense RBC suspension, owing to light scattering by RBCs and light absorption by hemoglobin. Instead, our method could be applied to studies of deformation and interactions of RBCs in microcirculation, to the design of microfluidic devices for blood diagnosis, and to predict the diffusion of solute and drug particles.

Acknowledgments

References

(1) Saadatmand, M., Ishikawa, T., Matsuki, N., Abdekhodaie, M.J., Imai, Y., Ueno, H., Yamaguchi, T., Fluid particle diffusion through high-hematocrit blood flow within a capillary tube, *Journal of Biomechanics,* Vol. 44, No. 1 (2011), pp. 170–175.

(2) Lima, R., Ishikawa, T., Imai, Y., Takeda, M., Wada, S., Yamaguchi, T., Measurement of individual red blood cell motions under high hematocrit conditions using a confocal micro-PTV system, *Annals of Biomedical Engineering*, Vol. 37 (2009), pp. 1546–1559.

(3) Hochmuth, R.M., Waugh, R.E., Erythrocyte membrane elasticity and viscosity, *Annual Review of Physiology*, Vol. 49 (1987), pp. 209–219.

(4) Fung, Y.C., Biodynamics: circulation, *Springer-Verlag*, New York (1984).

(5) Mohandas, N. and Evans, E., Mechanical properties of the red cell membrane in relation to molecular structure and genetic defects, *Annual Review of Biophysics and Biomolecular Structure*, Vol. 23 (1994), pp. 787-818.

(6) Evans, E.A., Bending elastic modulus of red blood cell membrane derived from buckling instability in micropipet aspiration tests, *Biophysical Journal*, Vol. 43 (1983), pp. 27–30.

(7) Doddi, S.K. and Bagchi, P., Three-dimensional computational modeling of multiple deformable cells flowing in microvessels, *Physical Review E*, Vol. 79 (2009), 046318.

(8) Dupin, M.M., Halliday, I., Care, C.M., Alboul, L., Munn, L.L., Modeling the flow of dense suspensions of deformable particles in three dimensions, *Physical Review E.*, Vol. 75 (2007), 066707.

(9) Zhao, H., Isfahani, A.H.G., Olson, L.N., Freund, J.B., A spectral boundary integral method for flowing blood cells, *Journal of Computational Physics*, Vol. 229 (2010), pp. 3726–3744.

(10) Fedosov, D.A., Caswell, B., Popel, A.S., Karniadakis, G.E., Blood flow and cell-free layer in microvessels, *Microcirculation*, Vol. 17 No. 8 (2010), pp. 615-28.

(11) Hoogerbrugge, P.J., Koelman, J.M.V.A., Simulating microscopic hydrodynamic phenomena with dissipative particle dynamics, *Europhysics Letters*, Vol. 19, No. 3 (1992), pp. 155–160.

(12) Pivkin, I.V., Karniadakis, G.E., Accurate coarse-grained modeling of red blood cells, *Physical Review Letters*, Vol. 101 (2008), 118105.

(13) Fedosov, D.A., Caswell, B. and Karniadakis, G.E., A multiscale red blood cell model with accurate mechanics, rheology, and dynamics, *Biophysical Journal*, Vol. 98 (2010), pp. 2215–2225.

(14) McWhirter, J.L., Noguchi, H., Gompper, G., Flow-induced clustering and alignment of vesicles and red blood cells in microcapillaries, *Proceedings of the National Academy of Science*, Vol. 106, (2009), pp. 6039–6043.

(15) Malevanets, A., Kapral., Mesoscopic model for solvent dynamics, *Journal of Chemical Physics* Vol. 110, (1999), pp.8605–8613.

(16) Bagchi, P., Mesoscale simulation of blood flow in small vessels, *Biophysical Journal*, Vol. 92, No. 6 (2007), pp. 1858–1877.

(17) Tanaka, N., Takano, T., Microscopic-scale simulation of blood flow using SPH method, *International Journal of Computational Methods*, Vol. 2, (2005), pp. 555-568.

(18) Tsubota, K., Wada, S., Yamaguchi, T., Particle method for computer simulation of red blood cell motion in blood flow, *Computer Methods and Programs in Biomedicine*, Vol. 83, (2006), pp. 139-146.

(19) Imai, Y., Kondo, H., Ishikawa, T., Yamaguchi, T., Modeling of hemodynamics arising from malaria infection, *Journal of Biomechanics*, Vol. 43, (2010), pp. 1386–1393.

(20) Imai, Y., Nakaaki, K., Kondo, H., Ishikawa, T., Lim, C.T., Yamaguchi, T., Margination of red blood cells infected by Plasmodium falciparum in a microvessel, *Journal of Biomechanics*, Vol. 44, (2011), pp. 1553–1558.

(21) Kamada, H., Imai, Y., Nakamura, M., Ishikawa, T., Yamaguchi, T., Computational analysis on the mechanical interaction between a thrombus and red blood cells: possible causes of membrane damage of red blood cells at microvessels, *Medical Engineering and Physics*, in press.

(22) Fåhræus, R., The suspension stability of the blood, *Physiological Reviews*, Vol. 9, (1929), pp. 241–274.

(23) Pozrikidis, C., Numerical simulation of the flow-induced deformation of red blood cells, *Annals of Biomedical Engineering*, Vol. 31, (2003), pp. 1194–1205.

(24) Koshizuka, S., Oka, Y., Moving-particle semi-implicit method for fragmentation of incompressible fluid, *Nucl Sci Eng*, Vol. 123, (1996), pp. 421–434.

(25) Suresh, S., Spatz, J., Mills, J.P., Micoulet, A., Dao, M., Lim, C.T., Beil, M., Seufferlein, T., Connection between single-cell biomechanics and human disease states: gastrointestinal cancer and malaria, *Acta Biomaterialia*, Vol. 1, (2005), pp. 15–30.

(26) Cranston, H.A., Boylan, C.W., Carroll, G.L., Sutera, S.P., Williamson, J.R., Gluzman, I.Y., Krogstad, D.J., Plasmodium falciparum maturation abolishes physiologic red cell deformability, *Science*, Vol. 223, (1984), pp.400–403.

(27) Gropp W, Lusk E, Skjellum A., Using MPI: portable parallel programming with the message-passing interface, *Cambridge: MIT Press*, (1999).

(28) Foster I. Designing and building parallel programs: concepts and tools for parallel software engineering, *New York: Addison-Wesley*, (1995).

(29) Goldsmith, H. L., Red cell motions and wall interactions in tube flow, *Federation Proceedings*, Vol. 30, (1971), pp. 1578–1590.

(30) Pries, A.R., Neuhaus, D., Gaehtgens, P., Blood viscosity in tube flow: dependence on diameter and hematocrit, *American Journal of Physiology*, Vol. 263, No. 6 (1992), pp. 1770-1778.

(31) Freund, J.B., Orescanin, M.M., Cellular flow in a small blood vessel, *Journal of Fluid Mechanics*, Vol. 671, (2011), pp. 466–490.

(32) Tateishi, N., Suzuki, Y., Soutani, M., Maeda, N., Flow dynamics of erythrocytes in microvessels of isolated rabbit mesentery: Cell-free layer and flow resistance, *Journal of Biomechanics*, Vol. 27, No. 9 (1994), pp. 1119–1125.

(33) Maeda, N., Suzuki, Y., Tanaka, J., Tateishi, N., Erythrocyte flow and elasticity of microvessels evaluated by marginal cell-free layer and flow resistance, *American Journal of Physiology*, Vol. 271, No. 6 (1996), pp. 2454-2461.

(34) Maeda, N., Erythrocyte rheology in microcirculation, *Japanese Journal of Physiology*, Vol. 46, (1996), pp. 1–14.

(35) Kim, S., Kong, R.L., Popel, A.S., Intaglietta, M., Johnson, P.C., A computer-based method for determination of the cell-free layer width in microcirculation, *Microcirculation*, Vol. 13, (2006), pp. 199–207.

(36) Kim, S., Kong, R.L., Popel, A.S., Intaglietta, M., Johnson, P.C., Temporal and spatial variations of cell-free layer width in arterioles, *American Journal of Physiology Heart and Circulatory Physiology*, Vol. 293, (2007), pp. 1526–1535.

(37) Bugliarello, G., Sevilla, J., Velocity distribution and other characteristics of steady and pulsatile blood flow in fine glass tubes, *Biorheology*, Vol. 7, No. 2 (1970), pp. 85–107.

(38) Reinke, W., Gaehtgens, P., and Johnson, P.C., Blood viscosity in small tubes: effect of shear rate, aggregation, and sedimentation, *American Journal of Physiology Heart and Circulatory Physiology*, Vol. 253, No. 3(1987), pp. 540–547.

(39) Pries, A.R., Ley, K., Claassen, M. and Gaehtgens P., Red cell distribution at microvascular bifurcations, *Microvascular Research*, Vol. 38, (1989), pp. 81-101.

(40) Pries, A.R., Secomb, T.W., Gessner, T., Sperandio, M.B., Gross, J.F. and Gaehtgens, P., Resistance to blood flow in microvessels in vivo, *Circulation Research*, Vol. 75, (1994), pp. 904-915.

(41) Sharan, M., Popel, A.S., A two-phase model for flow of blood in narrow tubes with increased effective viscosity near the wall, *Biorheology*, Vol. 38, No. 5-6 (2001), pp. 415-28.